



HAL
open science

Structural Effects of Cu,Zn Substitution in the Malachite–Rosasite System

Malte Behrens, Frank Girgsdies

► **To cite this version:**

Malte Behrens, Frank Girgsdies. Structural Effects of Cu,Zn Substitution in the Malachite–Rosasite System. *Journal of Inorganic and General Chemistry / Zeitschrift für anorganische und allgemeine Chemie*, 2010, 10.1002/zaac.201000028 . hal-00552444

HAL Id: hal-00552444

<https://hal.science/hal-00552444>

Submitted on 6 Jan 2011

HAL is a multi-disciplinary open access archive for the deposit and dissemination of scientific research documents, whether they are published or not. The documents may come from teaching and research institutions in France or abroad, or from public or private research centers.

L'archive ouverte pluridisciplinaire **HAL**, est destinée au dépôt et à la diffusion de documents scientifiques de niveau recherche, publiés ou non, émanant des établissements d'enseignement et de recherche français ou étrangers, des laboratoires publics ou privés.

**Structural Effects of Cu,Zn Substitution in the Malachite-
Rosasite System**

Journal:	<i>Zeitschrift für Anorganische und Allgemeine Chemie</i>
Manuscript ID:	zaac.201000028.R1
Wiley - Manuscript type:	Article
Date Submitted by the Author:	02-Mar-2010
Complete List of Authors:	Behrens, Malte; Fritz-Haber-Institute, Inorganic Chemistry Girgsdies, Frank; Fritz-Haber-Institute, Inorganic Chemistry
Keywords:	Cu/ZnO catalyst, Jahn-Teller distortions, Malachite, Rosasite



1
2
3
4
5
6
7
8
9
10
11
12
13
14
15
16
17
18
19
20
21
22
23
24
25
26
27
28
29
30
31
32
33
34
35
36
37
38
39
40
41
42
43
44
45
46
47
48
49
50
51
52
53
54
55
56
57
58
59
60

Structural Effects of Cu,Zn Substitution in the Malachite–Rosasite System

Malte Behrens^{a,*} and Frank Girgsdies^a

Dedicated to Professor Rüdiger Kniep on the Occasion of his 65th birthday

a) Fritz-Haber-Institut der Max-Planck-Gesellschaft
Abteilung Anorganische Chemie
Berlin, Germany

* Corresponding author: Dr. Malte Behrens
Fritz-Haber-Institut der Max-Planck-Gesellschaft
Abteilung Anorganische Chemie
Faradayweg 4-6
14195 Berlin
Germany

Email: behrens@fhi-berlin.mpg.de

Tel.: +49 30 8413-4408

Fax: +49 30 8413-4405

Abstract

Synthetic zincian malachite samples $(\text{Cu}_{1-x}\text{Zn}_x)_2(\text{OH})_2\text{CO}_3$ with $x = 0, 0.1, 0.2$ and 0.3 were characterized by powder X-ray diffraction and optical spectroscopy. The XRD patterns of the samples up to $x = 0.2$ indicate single phase materials with an approximately linear dependence of the refined lattice parameters on the Zn content. In contrast, the sample with a nominal Zn content $x = 0.3$ shows the formation of a small amount of aurichalcite $(\text{Zn,Cu})_5(\text{OH})_6(\text{CO}_3)_2$ as an additional phase. Based on the lattice parameter variations, the Zn content of the zincian malachite component in this sample is estimated to be $x \approx 0.27$, which seems to represent the maximum possible substitution in zincian malachite under the synthesis conditions applied. The results are discussed in relation to preparation of Cu/ZnO catalysts and the crystal structures of the minerals malachite and rosasite. One striking difference between these two structurally closely related phases is the orientation of the Jahn-Teller elongated axes of the CuO_6 octahedra in the unit cell, which seems to be correlated with the placement of the monoclinic β angle. The structural and chemical relationship between these crystallographically distinct phases is discussed using a hypothetical intermediate $\text{Zn}_2(\text{OH})_2\text{CO}_3$ phase of higher orthorhombic symmetry. In addition to the crystallographic analysis, optical spectroscopy proves to be a useful tool for estimation of the Cu:Zn ratio in $(\text{Cu}_{1-x}\text{Zn}_x)_2(\text{OH})_2\text{CO}_3$ samples.

Keywords

Malachite, Rosasite, Jahn-Teller distortions, Cu/ZnO catalyst

Introduction

Rosasite is a mineral of the chemical composition $(\text{Cu}_{1-x}\text{Zn}_x)_2(\text{OH})_2\text{CO}_3$ with approximately $0.3 < x < 0.5$. The related pure Cu mineral, $\text{Cu}_2(\text{OH})_2\text{CO}_3$, is malachite whose monoclinic crystal structure is reported in the literature [1]. While synthetic malachite can be easily prepared by precipitation, synthetic rosasite samples, i.e. single phase compounds with $x > 0.3$, are much harder to obtain, because usually aurichalcite, $(\text{Cu}_{1-x}\text{Zn}_x)_5(\text{OH})_6(\text{CO}_3)_2$ with $x > 0.5$, is formed if zinc-rich solutions are used for coprecipitation [2]. The cell parameters and space group of rosasite have been reported in

1
2
3 [3] and atomic coordinates were recently revealed on the basis of powder diffraction
4 studies [4]. Both malachite and roasite are monoclinic, space group $P2_1/a$ (No. 14),
5 crystallize in different crystal structures and are, thus, not isomorphous despite their
6 similar compositions. However, the close relation of the two phases is apparent from the
7 similar powder diffraction patterns (Fig. 1) and was recently discussed by Perchiazzi
8 [4,5]. It is interesting to note that roasite analogous minerals were found also with Mg,
9 Ni or Co instead of Zn together forming the roasite group of minerals.

10
11
12
13
14
15
16 These mixed basic transition metal carbonates have not only attracted the attention of
17 mineralogists, but also of solid state chemists active in the field of heterogeneous
18 catalysis, because $(\text{Cu}_{1-x}\text{Zn}_x)(\text{OH})_2\text{CO}_3$ is the relevant precursor compound for the
19 preparation of nanostructured Cu/ZnO catalysts [6-9]. Such catalysts are employed in
20 industrial synthesis of methanol from syngas, one of the top ten chemical processes
21 worldwide. A highly substituted synthetic roasite-like precursor would be desirable for
22 catalyst preparation, because the resulting Cu/ZnO material after calcination and
23 reduction is expected to exhibit a higher dispersion of the catalytically active Cu phase.
24 This is because the stabilizing function of the ZnO phase in the composite catalyst is
25 more efficient, if large amounts of Zn were homogeneously distributed in the cation lattice
26 of the precursor (Fig. 2) [6]. However, preparation of $(\text{Cu}_{1-x}\text{Zn}_x)(\text{OH})_2\text{CO}_3$ with
27 substitution levels near $x = 0.5$, i.e. as high as in natural roasite, remains a challenge and
28 values around $x = 0.3$ cannot be exceeded for state-of-the-art catalysts synthesized from
29 malachite/rosasite-like precursors. Zn-richer aurichalcite precursors were shown to lead
30 to inferior catalysts because aurichalcite is usually obtained in form of large platelets
31 exhibiting an unfavorable meso-structure compared to the needle-like zincian malachite.
32 We have started to investigate the structural properties of mixed basic Cu,Zn carbonates
33 from the perspective of Cu/ZnO catalyst preparation and first results have been reported
34 recently [2,6]. Here, we report on the effects of Cu by Zn substitution on the crystal
35 structure and optical absorption properties of malachite and discuss the relationship
36 between synthetic $(\text{Cu}_{1-x}\text{Zn}_x)(\text{OH})_2\text{CO}_3$ and to natural samples of malachite and roasite.
37
38
39
40
41
42
43
44
45
46
47
48
49
50
51
52

53 54 55 **Results and Discussion**

56
57
58
59
60

1
2
3
4
5
6
7
8
9
10
11
12
13
14
15
16
17
18
19
20
21
22
23
24
A comparison of the crystal structures of natural malachite [1] and rosasite [4] based on literature data, is shown in Figure 3. The main building blocks are $(\text{Cu,Zn})\text{O}_6$ octahedra and two distinct metal sites are present in both structures (Tab. 1). As pointed out by Perchiazzi [4], the view along the c -axis (Fig. 3, top row) shows equal connectivity of the octahedral units in both minerals in form of “double ribbons” of two edge-sharing octahedra running along $[001]$. The major structural difference of the two phases becomes apparent if the view is slightly tilted towards the (110) plane (Fig. 3, bottom row), showing that the monoclinic angle is placed between the short and the medium axes in malachite but between the short and the long axes in rosasite. Thus, one might get the idea that both in malachite and rosasite the monoclinic angle β is shifted towards 90° as the Cu:Zn ratio changes and that a hypothetical orthorhombic parent structure exists for both minerals, possibly at an intermediate value of x .

25
26
27
28
29
30
31
32
33
34
35
36
37
38
39
40
41
42
43
44
45
46
47
The effects of substitution of Cu by Zn on the crystal structure of synthetic malachite, leading to zincian malachite, $(\text{Cu}_{1-x}\text{Zn}_x)(\text{OH})_2\text{CO}_3$, were first investigated in detail by Porta et al. in 1988 [10,11]. The authors report a contraction of the unit cell and a systematic shift for the $h0l$ and hkl reflections. We have recently reported a characteristic and very pronounced shift of the $(20 -1)$ and $(21 -1)$ reflections to higher angles in the XRD patterns as Cu is gradually substituted by Zn [2]. The unusual effect on these characteristic XRD peaks was explained as a ligand field effect. In brief, the Jahn-Teller elongated axes of the CuO_6 octahedra in malachite exhibit an orientation nearly perpendicular to either the $(20 -1)$ or $(21 -1)$ lattice planes (Fig. 4). The unit cell is strongly contracted in the directions perpendicular to these planes as the Jahn-Teller ions Cu^{2+} are substituted with Zn^{2+} forming more regular octahedra. Thus, the d -spacing of these characteristic reflections can be used as a sensitive indicator for the degree of Zn incorporation in the malachite structure.

48
49
50
51
52
53
54
55
56
57
58
59
60
It remains, however, puzzling that certain reflections move strongly, while others remain more or less fixed (Fig. 5) despite their interrelation via the cell parameters. In particular, the intensive XRD peaks below $30^\circ 2\theta$, which are often used as fingerprint reflections for precursor phase identification in catalysis research, do hardly give information on the Cu:Zn ratio. This could be generally expected from the similar ionic radii of Cu^{2+} and Zn^{2+} , but at the same time the $(20 -1)$ and $(21 -1)$ peaks in the 2θ -range $31\text{--}33^\circ$ indicate

1
2
3 pronounced changes of the cell parameters. In addition, the low-angle reflections are not
4 suitable to unambiguously discriminate the malachite and rosasite structures in the
5 mineral phases (Fig. 1). This stimulated us to perform full pattern refinements of
6 synthetic zincian malachite samples with nominal molar Cu:Zn ratios of 100:0, 90:10,
7 80:20 and 70:30 using the mineral malachite as structural model. The samples were
8 synthesized according to established catalyst precursor preparation [12] by co-
9 precipitation and subsequent ageing of the precipitate in the mother liquor, during which
10 crystallization occurs. The Rietveld-fits are graphically shown in Figure 5 and selected
11 results are listed in Table 2. It is noted that the crystallinity of the materials decreased
12 with increasing Zn content. Furthermore, the 70:30 Zn sample contained aurichalcite as
13 an additional phase. For the single phase materials (samples up to $x = 0.2$), a full Rietveld
14 refinement of the atomic coordinates was possible and included in the fitting procedure.
15 In contrast, the poor crystallinity and presence of the aurichalcite by-phase did not allow
16 a reliable refinement of atomic positions for the 70:30 sample. Thus, fixed atomic
17 coordinates as obtained from the fit of the 80:20 sample were used in this case.

18
19
20
21
22
23
24
25
26
27
28
29
30
31
32
33
34
35
36
37
38
39
40
41
42
43
44
45
46
47
48
49
50
51
52
53
54
55
56
57
58
59
60
The unit cell volume and especially the b -axis of the synthetic malachite sample (Tab. 2)
were found to be slightly decreased in comparison to the natural samples (Tab. 1). The
Cu-Zn substitution in malachite leads to a Vegard-type linear trend for all lattice
parameters of $(\text{Cu}_{1-x}\text{Zn}_x)_2(\text{OH})_2\text{CO}_3$ in the range $0 < x < 0.2$ (Fig. 6). The a - and c -axes,
the monoclinic β angle as well as the unit cell volume (Tab. 2) decrease with increasing
Zn content, whereas the b -axis increase. These observations are in line with the results
reported by Porta et al. [11,12], who obtained phase pure zincian malachite samples for x
 ≤ 0.15 . The lattice parameters of their samples are in reasonable agreement with our
results and are also shown in Figure 6. It was discussed in [2] that the average contraction
of the Jahn-Teller elongated octahedra might be responsible for the cell volume
shrinking. The slightly larger ionic radius of Zn^{2+} and the elongation of the equatorial M-
O bonds are reflected in the increasing b -axis, but obviously do not compensate for the
shrinking effect. Porta et al. suggested that covalent shortening is responsible for the unit
cell volume contraction as the ionic Cu-O bond is substituted by more covalent Zn-O.

Porta et al. also discussed the non-systematic shift of certain groups of reflections [11].
The simultaneous anisotropic change of the lattice parameters causes only minor changes

1
2
3 in the XRD patterns, reflected strongly only in the positions of the (20 -1) and (21 -1)
4 reflections as discussed above. For instance, the shift of the well-resolved (200) reflection
5 near $19^\circ 2\theta$ is only hardly detected in the XRD patterns of the poorly crystalline catalyst
6 precursors (Fig 5), although the *a*-axis is significantly contracted (Fig. 6a). This is
7 because low-angle reflections generally shift less on the angular scale, but also, because
8 the effect of the contracted *a*-axis (-1.3% at $x \approx 0.3$) is to some extent compensated by the
9 simultaneous decrease of β leading to smaller changes in the *d*-spacing of the (*h*00)
10 planes of only -0.7%. These peculiarities are summarized in Figure 7 for the six most
11 intensive reflections of zincian malachite showing again the special sensitivity of the (20
12 -1) and (21 -1) peaks for the Cu:Zn ratio and the much smaller effect of the structural
13 changes on the other peaks, especially on the angular scale of a conventional Cu K_α
14 pattern (Fig. 7b).

15
16 The Zn content of the malachite-like phase fraction in the 70:30 sample was estimated on
17 basis of the linear trends shown in Figure 6. Linear regressions were performed using the
18 first three data points (single phase samples) for all four lattice parameters. The best
19 overall agreement for the lattice parameters of the zincian malachite phase in the fourth
20 sample is obtained when placing it at $x = 0.27$ (Fig. 6). This in the range $0.23 < x < 0.33$
21 suggested by Porta et al. on basis of the cell volume contraction [10,11] and in excellent
22 agreement with the limit of $x = 0.28$ determined from the shift of the (20 -1) reflection by
23 single peak fitting in a previous study [2]. It is noted, though, that the values scatter
24 between 0.25 (*b*-axis) to 0.28 (monoclinic β angle), if the Zn content was estimated for
25 each cell parameter separately.

26
27 As laboratory XRD provides no direct access to the distribution of Cu and Zn on the two
28 available metal sites in the malachite structure, the site preference has to be deduced
29 indirectly from the average distortion of the MO_6 coordination polyhedra in the structure.
30 Thus, distortion parameters Δ were calculated from the M-O distances *d* of the M1 and
31 M2 sites according to $\Delta = (1/6)\sum_{n=1,6}\{(d_n - \langle d \rangle) / \langle d \rangle\}^2$, with $\langle d \rangle$ being the average M-O
32 distance and d_n the individual distances (Fig. 6e, Tab. 1,2) [5,13]. It can be expected that
33 starting from the strongly Jahn-Teller distorted malachite structure, the parameter Δ
34 should decrease for a specific site upon successive substitution of Cu with Zn. It can be
35 seen in Figure 6e, that this is the case for the M2 site, while M1 does not show a clear
36
37
38
39
40
41
42
43
44
45
46
47
48
49
50
51
52
53
54
55
56
57
58
59
60

1
2
3 trend. Such a Zn ordering on the M2 site is also expected from ligand field
4 considerations, because (M2)O₆ is the initially less distorted polyhedron in pure
5 malachite (Tab. 1) and thus more suited for the coordination requirements of Zn²⁺. The
6 difference between the M1 and M2 sites is much more pronounced in natural malachite
7 compared to our synthetic material, i.e. the M1 site is more distorted and the M2 more
8 regular (Fig. 6e). This is possibly because a naturally formed mineral should be closer to
9 the thermodynamically favorable site distribution than a synthetic sample, which would
10 be influenced more strongly by randomizing kinetic factors. Consequently, site
11 preference upon Cu-Zn substitution can be expected to be more pronounced in minerals
12 than in synthetic samples. The M1:M2 ratio in the malachite unit cell is 1:1 and
13 extrapolation of Δ indicates that a hypothetical undistorted (M2)O₆ is present for Zn
14 contents around $x = 0.5$, suggesting that M2 is almost exclusively preferred by Zn also
15 for high substitution levels. This is also in good agreement with the distortion parameters
16 of (M2)O₆ calculated for natural rosasite (Tab. 1, Fig. 6e) and the site occupancy reported
17 by Perchiazzi [4,5]. However, it should be mentioned in this context that the two M2-O
18 bonds in rosasite, which are significantly longer than the remaining four (Tab. 1), are *cis*
19 to each other, and the resulting distortion Δ is not compatible with the *trans* geometry
20 expected for a Jahn-Teller distorted site.
21

22
23
24
25
26
27
28
29
30
31
32
33
34
35
36
37
38
39
40
41
42
43
44
45
46
47
48
49
50
51
52
53
54
55
56
57
58
59
60
Coming back to the structural relation of (zincian) malachite and rosasite, indeed an
evolution towards 90° is observed for the monoclinic angle β as Zn is incorporated into
malachite. However, it is clearly seen in Figure 6d that 90° is not reached at intermediate
values of x and that no such orthorhombic parent structure exists in between the regimes
of zincian malachite (up to $x \approx 0.3$) and rosasite ($0.3 < x < 0.5$). However, it is interesting
to note that the monoclinic angle of malachite indeed becomes 90° as it is extrapolated to
 $x = 1$ (Fig. 6d), suggesting a hypothetical orthorhombic Zn-only phase Zn₂(OH)₂CO₃,
which to our knowledge has not been reported so far. Following the highly idealized
trends shown in Figure 6e as dashed lines, such pure Zn₂(OH)₂CO₃ phase can be assumed
to consist of relatively regular octahedral building units due to the absence of Cu²⁺.
Starting from malachite, Zn substitution first occurs preferably on the M2 site until $x =$
0.5. Beyond this value, the M1 site is necessarily filled with Zn²⁺, leading to successive
decrease of the average distortions of the respective octahedra and, in the end, apparently

1
2
3 also of the monoclinic distortion of the unit cell. These considerations are highly
4 idealized, because other contributions than Jahn-Teller distortions that may contribute to
5 the monoclinic distortion of the unit cell are neglected. It is noted in this context that the
6 structures of the minerals pokrovskite [5] and chukanovite [14], $M_2(OH)_2CO_3$ with $M =$
7 Mg^{2+} and Fe^{2+} , respectively, can be refined in the monoclinic rosasite structure type
8 despite the absence of Jahn-Teller ions, suggesting an intrinsic monoclinic distortion of
9 these minerals. Interestingly, a sub-stoichiometric occupation of the cation sites was
10 reported for the former and could not be excluded for the latter mineral.
11

12 However, the simplified picture of hypothetical, undistorted, orthorhombic $Zn_2(OH)_2CO_3$
13 allows an “inverse” gedankenexperiment, in which malachite and rosasite are derived
14 from such common $Zn_2(OH)_2CO_3$ phase as starting material. Assuming Cu-Zn ordering
15 for both phases, the M1 site would be gradually filled with Cu^{2+} now introducing Jahn-
16 Teller elongation of given axial M1-O bonds in the initially almost undistorted octahedra.
17 In this situation, different possibilities for the orientation of these elongated axes in the
18 unit cell exist, as there is the choice between the three orthogonal four-fold rotation axes
19 of the $M1O_6$ octahedra. This leads to the principal difference of the malachite and the
20 rosasite structure as can be seen in Figure 8 showing both crystal structures along their
21 crystallographic axes. It is noted that because of the different orientation of the
22 monoclinic angles, and according to crystallographic convention, requiring the b -axis to
23 be the monoclinic axis, the a -axis of malachite corresponds to the b -axis of rosasite, and
24 vice versa. Thus, the [010] view of malachite is analogous to the [100] view of rosasite
25 (Fig. 8, top row), while the structural situation in malachite viewed along [100] is
26 represented in the [010] view of rosasite (Fig. 8, center row).
27

28 The Jahn-Teller elongated bonds of the CuO_6 polyhedra of those metal sites which are
29 mainly occupied by Cu (M1 and M2 in malachite and M1 in rosasite) are emphasized in
30 black in Figure 8. It can be seen that, when viewed along the long axes (top row), their
31 projections are aligned almost in parallel in malachite, while they exhibit a nearly
32 perpendicular zig-zag arrangement in rosasite. Conversely, when viewed along the
33 medium axes (center row), they are almost parallel in rosasite and a little staggered in
34 malachite, still being far away from a rectangular arrangement. At low Cu:Zn ratios, i.e.
35 if the Jahn-Teller distorted units are diluted, the perpendicular zig-zig arrangement
36
37
38
39
40
41
42
43
44
45
46
47
48
49
50
51
52
53
54
55
56
57
58
59
60

1
2
3 (rosasite structure) seems to be favorable, while at high Cu:Zn ratios, i.e. if the Jahn-
4 Teller distortions are concentrated, a more parallel orientation seems to be more stable
5 resulting in the malachite structure. Thus, the hypothetical $Zn_2(OH)_2CO_3$ phase helps to
6 understand the existence of different non-isomorphous structures for malachite and
7 rosasite despite their similar composition and crystallization in the same class of space
8 groups. In this context, the projections in Figure 8 are very suggestive, as it appears that
9 the different monoclinic distortion in both minerals can be explained by the direction of
10 parallel orientation of the projected Jahn-Teller elongations opening the respective angle
11 to $> 90^\circ$ (top row, left and center row right). Finally, the differences of the malachite and
12 rosasite structures can also be seen in the view along the short axis if the elongated bonds
13 are considered (bottom row). In rosasite, the Jahn-Teller elongated bonds of $(M1)O_6$
14 point to the same carbonate ligand, while for malachite there is only one black bond per
15 carbonate anion.
16
17
18
19
20
21
22
23
24
25

26 While the XRD pattern of our mineral malachite sample could be fitted easily (Tab. 1,
27 Fig. 1), we encountered problems in the attempt to refine the rosasite structure. Due to
28 anisotropic peak broadening, no satisfying agreement of calculated and experimental
29 pattern could be obtained. Furthermore, preliminary results using only the rosasite
30 structure suggested presence of an additional phase since it could not account for two
31 weak reflections at 31.9 and $32.9^\circ 2\theta$, which have been already mentioned in [2] and are
32 marked in Figure 1b. The fit became significantly better, though still not good enough for
33 a reliable refinement of the atomic positions, when an additional (zincian) malachite
34 phase was introduced as has been suggested in [2]. In Figure 1b only the resulting peak
35 positions of such two phase fit are shown and the corresponding cell parameters are given
36 in Table 1, showing that it is possible to have a mixture of the zincian malachite and
37 rosasite phases, in which most of the well-resolved and intense XRD reflections overlap
38 resulting in complex peak profiles. The $(20 -1)$ and $(21 -1)$ peaks of malachite are the
39 striking exception among the intense reflections and the most obvious indication of the
40 malachite-like phase fraction. It either is present as a separated impurity phase or as
41 domains in the rosasite crystals resulting from fluctuations of the Zn content. On the basis
42 of the linear trends shown in Figure 6, the Zn content x of this fraction of the mineral
43 sample can be estimated to ca. 0.18 falling clearly below the average value of 0.38
44
45
46
47
48
49
50
51
52
53
54
55
56
57
58
59
60

1
2
3 determined by EDX. It is noted, though, that the scattering among the individual lattice
4 constant was in the range $0.13 < x < 0.25$.
5

6
7 As a complementary technique, optical absorption spectroscopy was applied for natural
8 as well as synthetic samples with nominal Zn contents of $x = 0, 0.1$ and 0.3 . The spectra
9 are shown in Figure 9. As expected, those of natural and synthetic malachite are similar.
10 For malachite two major contributions are observed, an intensive band centered around
11 810 nm and a shoulder at lower energies near 1150 nm. These are typical features of
12 tetragonally distorted octahedral CuO_6 chromophors [15-17]. Significant changes can be
13 observed as the Zn content of the samples is increased. The subtle change of the color of
14 the samples from green to bluish green is caused by a slight blue-shift of the former band
15 into the vis-range of the spectrum and development of a shoulder at high energy seen
16 most clearly in the spectrum of rosasite (indicated by an arrow in Fig. 9). However, the
17 changes are much more pronounced at lower energy in the NIR. This spectral range was
18 reported to be suitable for discrimination of rosasite group minerals [18]. The band at
19 1150 nm was assigned to the ${}^2\text{B}_{1g} \rightarrow {}^2\text{A}_{1g}$ transition of Cu^{2+} [18] and its relative intensity
20 decreases as copper is substituted by optically silent Zn^{2+} . The band is also shifted to
21 lower energies, which may be associated with the geometrical effect of the Zn^{2+} ions on
22 the MO_6 polyhedra as shown above in Figure 6e affecting also the CuO_6 chromophors.
23 The rough correlation of the position of this band with the Zn content (Fig. 10) renders
24 optical spectroscopy in the range > 1000 nm an alternative tool for convenient estimation
25 of the Cu:Zn ratio in zincian malachite, which is not affected by the crystallographic
26 differences of malachite and rosasite.
27

28
29 In summary, these results suggest a relative phase stability of mixed Cu,Zn basic
30 carbonates as shown in the simplified free energy diagram in Figure 11. At $x = 0$,
31 malachite is the most stable phase and synthetically easily accessible. As x increases low
32 amount of Cu in malachite can be substituted by Zn leading to zincian malachite (black
33 curve in Fig. 11). At a critical composition, no more Zn can be incorporated into zincian
34 malachite and formation of a phase mixture of zincian malachite and aurichalcite is
35 energetically favorable. The reason is most probably the increasing concentration of
36 regular MO_6 octahedra, which destabilizes the aligned arrangement of the Jahn-Teller
37 distortions present in malachite. Aurichalcite (light grey curve) exhibits a higher
38
39
40
41
42
43
44
45
46
47
48
49
50
51
52
53
54
55
56
57
58
59
60

1
2
3 variability of building units [19], e.g. also tetrahedrally coordinated and almost
4 undistorted octahedral sites are available, which can accommodate Zn ions [20].
5

6
7 Under the synthesis conditions applied for this study the critical composition is at $x =$
8 0.27 and the two-phase regime lasts until x ca. 0.5 [21]. It is noted that these values
9 strongly depend on the exact setting of the synthesis conditions like pH, temperature and
10 ageing time, but also on the general mode of co-precipitation. For instance, if the
11 decreasing pH technique is used at otherwise the same conditions, the critical
12 composition cannot exceed $x = 0.11$ [2] and the two-phase regime ends at approximately
13 $x = 0.60$ [21]. Thus, the relative positions of the curves in Figure 11, which were chosen
14 to qualitatively agree with thermodynamical data reported in literature [22], are a
15 function of the synthesis parameters indicating that the applied method of preparation
16 does not necessarily lead to equilibrium phases.
17

18
19 Rosasite seems to be metastable towards zincian malachite and/or aurichalcite at all
20 compositions (dark grey curve) as it is not accessible by the co-precipitation and ageing
21 procedure. According to the above considerations the curves of zincian malachite and
22 rosasite should meet at $x = 1$, the hypothetical common $\text{Zn}_2(\text{OH})_2\text{CO}_3$ phase. Anyway,
23 rosasite is accessible under naturally occurring mineralization conditions for compositions
24 $0.3 < x < 0.5$.
25

26
27 Consequences of the situation depicted in Figure 11 for preparation and optimization of
28 Cu/ZnO catalysts relate to the observation that a coarse relationship between the Zn
29 content x in $(\text{Cu}_{1-x}\text{Zn}_x)(\text{OH})_2\text{CO}_3$ and the catalytic activity of the resulting Cu/ZnO
30 catalyst exists [6]. Near the critical limit of 0.27 a maximum of gas accessible Cu surface
31 areas, i.e. highest dispersion of Cu, was observed due to an efficient nano-structuring of
32 the precursor upon thermal treatment (Fig. 2). At $x > 0.27$, aurichalcite is formed as a by-
33 phase and the decreasing catalytic activity is attributed to the unfavorable meso-structure
34 of this precursor phase leading to undesired embedment of the active Cu particles. Thus,
35 synthesis conditions have to be found, which either drive the critical composition of
36 zincian malachite beyond $x = 0.27$ by lowering the black curve or make rosasite-like
37 precursors accessible by lowering the dark grey curve.
38
39
40
41
42
43
44
45
46
47
48
49
50
51
52
53
54

55 56 57 **Conclusion** 58 59 60

1
2
3 The main conclusions of this work are: (i) Malachite and rosasite, $(\text{Cu}_{1-x}\text{Zn}_x)(\text{OH})_2\text{CO}_3$,
4 which are not boundary cases of an isomorphous substitution series [4], can be envisaged
5 as two alternative distortions of a hypothetical common orthorhombic parent structure as
6 a function of Cu:Zn ratio. Synthetic samples with a Zn content of up to $x = 0.27$ adopt the
7 malachite-like structure, which exhibits a more coaxial arrangement of the Jahn-Teller
8 distorted polyhedra and, thus, seems not to be able to incorporate larger amounts of
9 preferably symmetrically coordinated Zn^{2+} ions. (ii) As expected, Zn preferably occupies
10 the less distorted M2 site in synthetic zincian malachite and Cu-Zn substitution leads to
11 anisotropic, but linear Vegard-type changes of the malachite lattice constants, which due
12 to a compensating effect are hardly reflected in the peak positions of most XRD
13 reflections. (iii) In natural samples both phases may co-exist, possibly as domains with
14 different Zn contents. This phase co-existence may be difficult to see by powder XRD,
15 because the individual patterns are very similar and differ only in a few selected
16 reflections. (iv) In addition to full pattern refinement or analysis of the d-spacing of the
17 characteristic (20 -1) or (21 -1) peaks [2], optical spectroscopy can be applied to estimate
18 the Cu:Zn ratio in zincian malachite catalyst precursors.

32 33 **Experimental**

34 Mineral samples were obtained from the mineral collection of the Technical University
35 Berlin. Elemental analysis by EDX revealed a Zn content x of 0.38 for the rosasite
36 sample [2]. In case of malachite, EDX showed that in the mineral sample 7% of the
37 cations were Al^{3+} or Si^{4+} , which are probably present in an impurity phase not seen by
38 XRD. However, another 2% are Mg^{2+} , which could possibly reside on the Cu sites in the
39 malachite structure. Further analyses of the minerals like TG and IR spectroscopic
40 investigations can be found in [2]. The series of synthetic zincian malachite samples was
41 prepared with varying molar Cu/Zn ratios of 100:0, 90:10, 80:20 and 70:30 by constant-
42 pH co-precipitation and some results were presented in earlier contributions [2,6,21].
43 Co-precipitates were obtained by co-feeding mixed metal nitrate and soda solutions at pH
44 7 and $T = 65$ °C. The initially amorphous precipitates (zincian georgeite [23]) were aged
45 in the mother liquor for 2 h. During ageing crystallization occurred and the solids were
46
47
48
49
50
51
52
53
54
55
56
57
58
59
60

1
2
3 recovered by filtration, washing and drying. Further details on the preparation process
4 can be found in ref. [21] and [6].
5

6
7 For the synthetic samples, the X-ray diffraction (XRD) measurements were performed on
8 a STOE STADI P transmission diffractometer equipped with a primary focusing Ge
9 monochromator (Cu $K\alpha_1$ radiation) and a curved position sensitive detector (static mode,
10 resolution 0.03° , accumulation time 1800 s). The sample powders were filled into 0.3 mm
11 diameter glass capillaries and mounted on a capillary sample holder which was rotated
12 around the capillary axis during measurement. The mineral samples were measured on
13 the same setup, except that a linear position sensitive detector was used (moving mode,
14 step size 0.1° , counting time 10 s/step, resolution 0.01° , total accumulation time 634 s)
15 and the samples were mounted in the form of a clamped sandwich of small amounts of
16 powder fixed with a small amount of grease between two layers of thin polyacetate film.
17 Refinements were done in the 2θ range $5\text{--}90^\circ$ using the software package TOPAS [24].
18 Only 2θ -sections of $10\text{--}50^\circ$ are shown in the figures for clarity. The background for the
19 mineral samples was modelled using a third order Chebychev polynomial, while the
20 synthetic samples required a second order Chebychev polynomial plus a very broad
21 (FWHM $> 5^\circ 2\theta$) Gaussian peak around $25\text{--}30^\circ 2\theta$ to account for the diffuse scattering
22 caused by the glass capillary walls. Details of the refinements are given in Table 3.
23

24
25 Diffuse reflectance UV–vis–NIR spectroscopy was performed using a PerkinElmer
26 Lambda 950 spectrometer equipped with a Harrick Praying Mantis DRP-P72 accessory
27 and HVC-VUV reaction chamber. The spectra of selected samples were measured in the
28 spectral range 250–2500 nm at room temperature in static air. For the background
29 correction the Spectralon reflectance standard (Labsphere) was used. All spectroscopic
30 measurements were carried out sequentially with a scan speed of 266 nm min^{-1} , a
31 nominal slit width of 2.5 nm, a response time of 0.20 s, and a step width of 1 nm. The
32 apparent absorption $K(\lambda)$ as a function of the wavelength λ was evaluated from the
33 diffuse reflectance data using the Kubelka-Munk equation.
34
35

36 37 38 39 40 41 42 43 44 45 46 47 48 49 50 51 52 53 54 **Acknowledgements**

55 We thank Nicole Giliard and the Technical University Berlin for providing the mineral
56 reference samples, Edith Kitzelmann for XRD measurements, Gisela Weinberg for EDX
57
58
59
60

1
2
3 analyses and Genka Tzolova-Müller for recording the optical spectra. Sophia Klokishner,
4 Oleg Reu, Igor Kasatkin, Annette Trunschke and Robert Glaum are acknowledged for
5 fruitful discussion of the spectroscopic results. Financial support was given by the BMBF
6 (Förderkennzeichen 01RI0529). Robert Schlögl is greatly acknowledged for his
7 continuous support.
8
9
10
11
12
13
14
15
16
17
18
19
20
21
22
23
24
25
26
27
28
29
30
31
32
33
34
35
36
37
38
39
40
41
42
43
44
45
46
47
48
49
50
51
52
53
54
55
56
57
58
59
60

Figure Captions

Figure 1: Sections of the experimental and calculated powder XRD patterns of a natural sample of malachite (a) (dots: experimental data, blue line: calculated pattern, green line: background, bottom curve: difference plot, ticks: peak positions). Sections of the experimental pattern and refined peak positions (red ticks: malachite, black ticks: rosasite) of the rosasite sample (b). The (20 -1) and (21 -1) reflections of malachite are marked.

Figure 2: Cartoon of precursor nano-structuring upon thermal treatment (calcination and reduction) during Cu/ZnO catalyst synthesis: Needle-like $(\text{Cu}_{1-x}\text{Zn}_x)_2(\text{OH})_2\text{CO}_3$ crystals decompose and de-mix into Cu- and ZnO resulting in a nano-particulate Cu/ZnO composite [6], which is shown as HRTEM image for a catalyst with a Cu:Zn ratio of 70:30 [25]. Nano-structuring is more efficient at x near 0.5.

Figure 3: Comparison of the crystal structures of malachite (left) and rosasite (right). A view along the [001] direction (top row) emphasizes their close relationship, while a slight change of the viewing angle onto the (001) plane reveals the different placement of the monoclinic angles (bottom row).

Figure 4: Unit cell of malachite, slightly tilted view towards (50 -1). Only the Jahn-Teller elongated bonds of the CuO_6 units are shown. They are oriented either perpendicular to (20 -1) (shown in blue) or to (21 -1) (shown in green). The directions of strongest unit cell contraction upon Cu-Zn substitution are indicated by arrows. Carbonate groups were omitted for clarity.

Figure 4: Sections of the experimental and calculated XRD patterns of synthetic zincian malachite with nominal Cu:Zn ratios of 100:0 (a), 90:10 (b), 80:20 (c) and 70:30 (d); the different extent of peak shifts is indicated by vertical lines for selected reflections (dots: experimental data, black line: calculated patterns, grey line: background, bottom curve:

1
2
3 difference plot, ticks: peak positions; the two most intensive aurichalcite reflections are
4 marked in (d) and the aurichalcite peak positions are shown in green)
5
6
7

8
9 Figure 5: Trends of lattice parameters a (a), b (b), c (c), β (d) and the distortion parameter
10 Δ (e) of synthetic zincian malachite as a function of Zn content. The data represented as
11 circles was taken from [11]. Open symbols in (d) refer to reference data for mineral
12 samples from Table 1 (squares: this study, triangles: literature data of Tab. 1).
13
14
15
16

17
18 Figure 6: Changes in the powder XRD pattern of zincian malachite samples as a function
19 of Zn content x for the six most intensive reflections
20
21
22

23 Figure 7: Correlation between the orientation of the Jahn-Teller elongated Cu-O bonds
24 (emphasized in black) and the direction of the monoclinic distortion of the unit cell for
25 malachite (left) and rosasite (right), viewed along the long (top row), middle (center row)
26 and short (bottom row) unit cell axes.
27
28
29
30
31

32 Figure 8: Optical absorption spectra in the UV-vis-NIR range of the minerals malachite
33 (a) and rosasite (e) and of the synthetic zincian malachite samples with 100% (b), 90%
34 (c), and 70% Cu (d). The grey bars mark the position of the low-energy band determined
35 from a simple fit the range 500-2100 nm with two Gaussians.
36
37
38
39
40

41 Figure 9: Position of the low energy band on the wavelength-scale in the optical
42 absorption spectra of $(\text{Cu}_{1-x}\text{Zn}_x)_2(\text{OH})_2\text{CO}_3$ samples as a function of Zn content. The
43 contribution of the minor amount of by-phases in the two Zn-richest samples (see text)
44 has been neglected.
45
46
47
48

49 Figure 10: Proposed energetic situation of the basic carbonate systems
50 $(\text{Cu}_{1-x}\text{Zn}_x)(\text{OH})_2\text{CO}_3$ and $(\text{Cu}_{1-x}\text{Zn}_x)_5(\text{OH})_6(\text{CO}_3)_2$, which are important in the context of
51 Cu/ZnO catalyst synthesis. This representation is strongly idealized and neglects, e.g.,
52 differences in anion composition.
53
54
55
56
57
58
59
60

1
2
3
4
5
6
7
8
9
10
11
12
13
14
15
16
17
18
19
20
21
22
23
24
25
26
27
28
29
30
31
32
33
34
35
36
37
38
39
40
41
42
43
44
45
46
47
48
49
50
51
52
53
54
55
56
57
58
59
60

Tables

Table 1: Comparison of structural data of natural malachite and rosasite samples reported in literature and in this study. Our rosasite sample contains rosasite as main phase, but also a minor malachite-like fraction (see text). The two longest bonds in each set are emphasized in bold.

	Malachite	Rosasite	Malachite sample	Rosasite sample	
				Rosasite	Malachite
Reference	[1]	[4,5] ^{a)}	<i>this study</i>	<i>this study</i>	
a / Å	9.502	12.2413(2)	9.4988(4)	12.2266(15)	9.443(3)
b / Å	11.974	9.3705(2)	11.9663(5)	9.3617(10)	12.080(4)
c / Å	3.240	3.1612(2)	3.24553(11)	3.1595(3)	3.2037(7)
β / °	98.75	98.730(3)	98.636(2)	98.697(8)	97.358(13)
V / Å ³	364.35	357.90	364.72(3)	357.48(6)	362.46(19)
M1-O4 / Å	1.898(1)	1.952(9)	1.910(10)	<i>n.d.</i>	<i>n.d.</i>
M1-O5 / Å	1.911(1)	1.89(1)	1.950(9)	<i>n.d.</i>	<i>n.d.</i>
M1-O1 / Å	1.996(1)	2.078(8)	1.966(11)	<i>n.d.</i>	<i>n.d.</i>
M1-O2 / Å	2.055(1)	2.057(5)	2.154(13)	<i>n.d.</i>	<i>n.d.</i>
M1-O1 / Å	2.509(1)	2.443(7)	2.610(13)	<i>n.d.</i>	<i>n.d.</i>
M1-O2 / Å	2.642(1)	2.519(3)	2.649(15)	<i>n.d.</i>	<i>n.d.</i>
Δ_{M1}	0.0185	0.0123	0.0196	<i>n.d.</i>	<i>n.d.</i>
M2-O4 / Å	1.918(1)	2.01(1)	1.970(12)	<i>n.d.</i>	<i>n.d.</i>
M2-O5 / Å	1.915(1)	2.07(1)	1.955(11)	<i>n.d.</i>	<i>n.d.</i>
M2-O3 / Å	2.049(1)	2.046(3)	1.952(11)	<i>n.d.</i>	<i>n.d.</i>
M2-O2 / Å	2.115(1)	2.256(3)	2.150(11)	<i>n.d.</i>	<i>n.d.</i>
M2-O5 / Å	2.369(1)	2.251(1)	2.473(13)	<i>n.d.</i>	<i>n.d.</i>
M2-O4 / Å	2.372(1)	2.16(1)	2.428(14)	<i>n.d.</i>	<i>n.d.</i>
Δ_{M2}	0.0079	0.0044	0.0105	<i>n.d.</i>	<i>n.d.</i>

^{a)} Bond lengths were taken from reference [4], while the cell parameters are based for the transformed unit cell given in [5]; *n.d.* = not determined

Table 2: Selected results from the Rietveld refinement of the synthetic zincian malachite samples. The two longest bonds in each set are emphasized in bold.

Zn content x	0	0.1	0.2	≈ 0.27
$a / \text{\AA}$	9.4938(9)	9.44900(3)	9.4030(7)	9.37228(19)
$b / \text{\AA}$	11.9086(11)	11.9749(14)	12.0290(9)	12.060(3)
$c / \text{\AA}$	3.2457(3)	3.2198(3)	3.1983(2)	3.1801(5)
$\beta / ^\circ$	98.684(5)	97.839(6)	96.889(4)	96.190(12)
$V / \text{\AA}^3$	362.75(5)	360.92(5)	359.15(4)	357.36(12)
M1-O4 / \AA	1.914(15)	1.898(15)	1.926(11)	<i>n.d.</i>
M1-O1 / \AA	2.020(16)	1.985(4)	2.017(13)	<i>n.d.</i>
M1-O5 / \AA	2.025(12)	2.057(4)	1.968(11)	<i>n.d.</i>
M1-O2 / \AA	2.097(18)	2.125(5)	2.066(11)	<i>n.d.</i>
M1-O1 / \AA	2.559(18)	2.428(4)	2.404(14)	<i>n.d.</i>
M1-O2 / \AA	2.66(2)	2.786(6)	2.689(14)	<i>n.d.</i>
Δ_{M1}	0.0170	0.0190	0.0161	<i>n.d.</i>
M2-O4 / \AA	1.784(18)	1.855(5)	1.841(14)	<i>n.d.</i>
M2-O5 / \AA	1.911(18)	1.954(19)	1.993(13)	<i>n.d.</i>
M2-O3 / \AA	2.078(15)	1.974(9)	2.011(12)	<i>n.d.</i>
M2-O2 / \AA	2.082(15)	2.143(3)	2.087(10)	<i>n.d.</i>
M2-O5 / \AA	2.42(2)	2.47(2)	2.347(14)	<i>n.d.</i>
M2-O4 / \AA	2.51(2)	2.406(5)	2.355(16)	<i>n.d.</i>
Δ_{M2}	0.0148	0.0118	0.0080	<i>n.d.</i>

n.d. = not determined

Table 3: Technical details of the Rietveld refinements

	x = 0	x = 0.1	x = 0.2	x ≈ 0.27	malachite (mineral)
R_{exp}^a	0.0158	0.0164	0.0150	0.0152	0.0753
R_{wp}^a	0.0406	0.0265	0.0256	0.0264	0.0920
R_p^a	0.0308	0.0209	0.0204	0.0207	0.0689
$R_{exp}'^a$	0.0361	0.0574	0.0352	0.0399	0.1701
$R_{wp}'^a$	0.0928	0.0932	0.0602	0.0696	0.2079
R_p^a	0.0813	0.0867	0.0547	0.0609	0.2152
GOF	2.57	1.62	1.71	1.74	1.22
R_{Bragg}	0.01060	0.00846	0.00452	0.00561	0.02989
No. of reflections	225	224	222	221	226
No. of parameters	57	57	57	39	51

^a Primed R values are background corrected; definition of the R values according to [26].

References

- [1] F. Zigan, W. Josig, H. D. Schuster, *Z. Kristallogr.* **1977**, *145*, 412.
- [2] M. Behrens, F. Girgsdies, A. Trunschke, R. Schlögl, *Eur. J. Inorg. Chem.* **2009**, *10*, 1347.
- [3] A. C. Roberts, J. L. Jambor, J. D. Grice, *Powd. Diff.* **1986**, *1*, 56.
- [4] N. Perchiazzi, *Z. Kristallogr. Suppl.* **2006**, *23*, 505.
- [5] N. Perchiazzi, S. Merlino, *Eur. J. Mineral.* **2006**, *18*, 787.
- [6] M. Behrens, *J. Catal.* **2009**, *267*, 24.
- [7] D. Waller, D. Stirling, F. S. Stone, M. S. Spencer, *Faraday Discuss. Chem. Soc.* **1989**, *87*, 107.
- [8] T. Fujitani, J. Nakamura, *Catal. Lett.* **1998**, *56*, 119.
- [9] R. G. Herman, K. Klier, G. W. Simmons, B. P. Finn, J. B. Bulko, T. P. Kobylinski, *J. Catal.* **1979**, *56*, 437.
- [10] P. Porta, G. Fierro, M. Lo Jancono, G. Moretti, *Catal. Today* **1988**, *2*, 675.
- [11] P. Porta, S. De Rossi, G. Ferraris, M. Lo Jacono, G. Minelli, G. Moretti, *J. Catal.* **1988**, *109*, 367.
- [12] S. Schimpf, M. Muhler in *Synthesis of Solid Catalysts* ed. K. P. de Jong, Wiley-VCH., Weinheim, **2009**, 329 ff.
- [13] R. K. Eby, F. C. Hawthorne, *Acta Cryst.* **1993**, *B49*, 28.
- [14] I. V. Pekov, N. Perchiazzi, S. Merlino, V. N. Kalachev, M. Merlini, A. E. Zadov, *Eur. J. Mineral.* **2007**, *19*, 891.
- [15] B. J. Hathaway, D. E. Billing, *Coord. Chem. Rev.* **1970**, *5*, 143.
- [16] K. M. Reddy, A. S. Jacobs, B. J. Reddy, Y. P. Reddy, *Phys. Status Solidi* **1987**, *B139*, K145.
- [17] R. Glaum, M. Weil, D. Özalp, *Z. Anorg. Allg. Chem.* **1996**, *622*, 1839
- [18] R. L. Frost, B. J. Reddy, D. L. Wain, W. N. Martens, *Spectrochim. Acta* **2007**, *A66*, 1075.
- [19] M. M. Harding, B. M. Kaiuki, R. Cernik, G. Cressey, *Acta Cryst B.* **1994**, *50*, 673.
- [20] J. M. Charnock, P. F. Schofield, C. M. B. Henderson, G. Cressey, B. A. Cressey, *Mineral. Mag.*, **1996**, *60*, 887.

- 1
2
3
4 [21] B. Bems, M. Schur, A. Dassenoy, H. Junkes, D. Herein, R. Schlögl, *Chem. Eur. J.*
5 **2003**, 9, 2039.
6
7 [22] A. K. Alwan, J. H. Thomas, P. A. Williams, *Transition Met. Chem.* **1980**, 5, 3.
8
9 [23] A. M. Pollard, M. S. Spencer, R. G. Thomas, P. A. Williams, J. Holt, J. R.
10 Jennings, *Appl. Catal. A* **1992**, 85, 1.
11
12 [24] A. A. Coelho, *Topas, General Profile and Structure Analysis Software for*
13 *Powder Diffraction Data*, Version 3.0, Bruker AXS GmbH, Karlsruhe, Germany,
14 **2006**.
15
16 [25] I. Kasatkin, P. Kurr, B. Kniep, A Trunschke, R. Schlögl, *Angew. Chem.* **2007**,
17 *119*, 7465.
18
19 [26] R. A. Young in *The Rietveld Method*, ed. R.A. Young, Oxford University Press
20 **1993**, 1 ff.
21
22
23
24
25
26
27
28
29
30
31
32
33
34
35
36
37
38
39
40
41
42
43
44
45
46
47
48
49
50
51
52
53
54
55
56
57
58
59
60

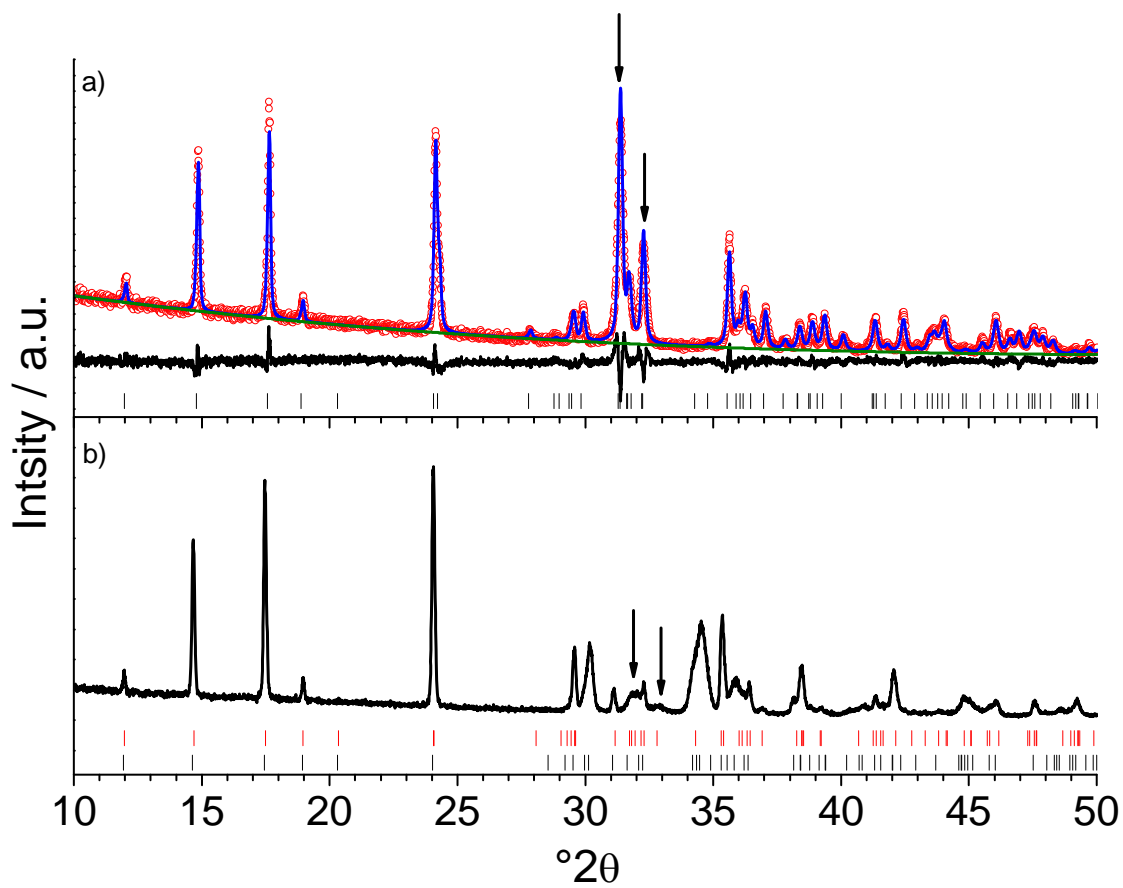


Figure 1

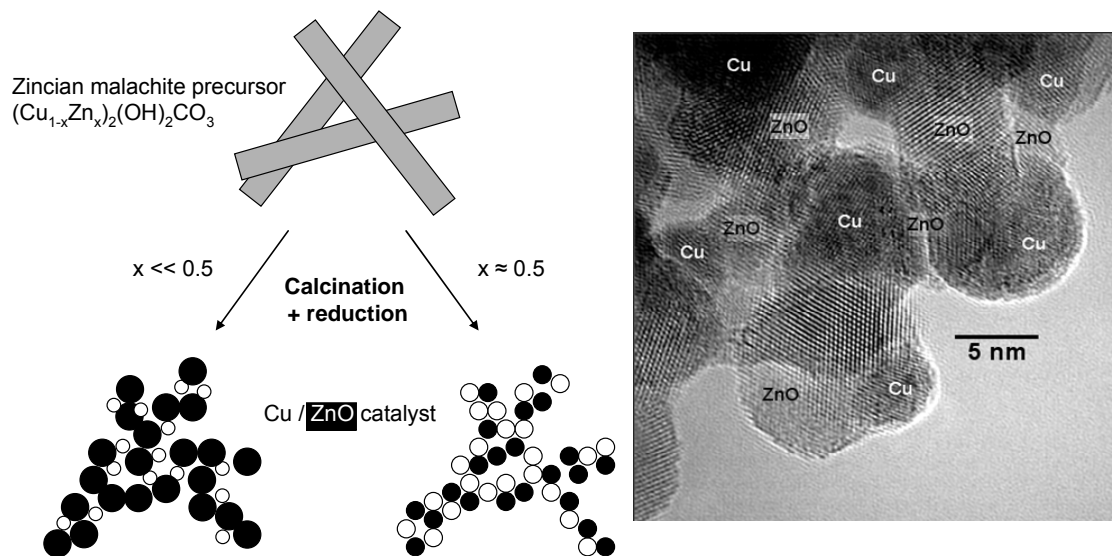


Figure 2

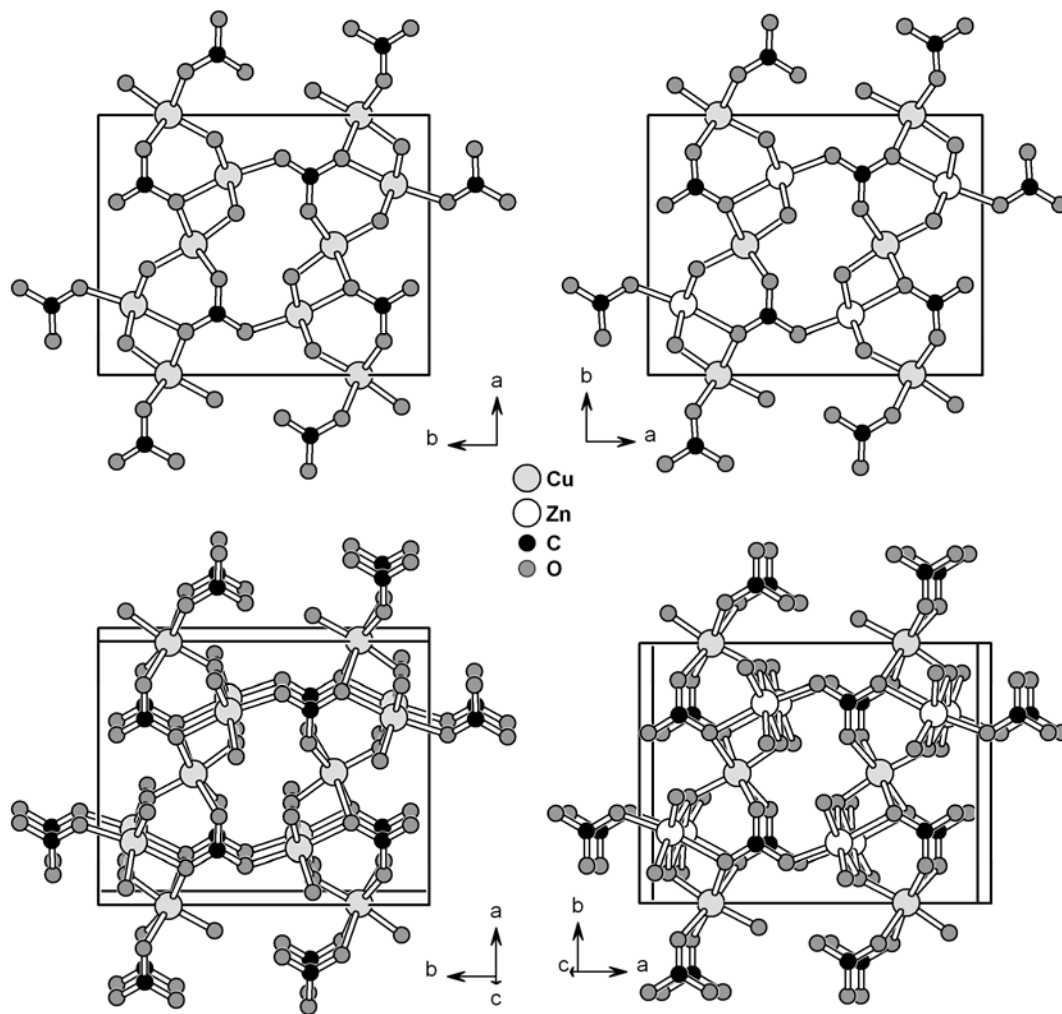


Figure 3

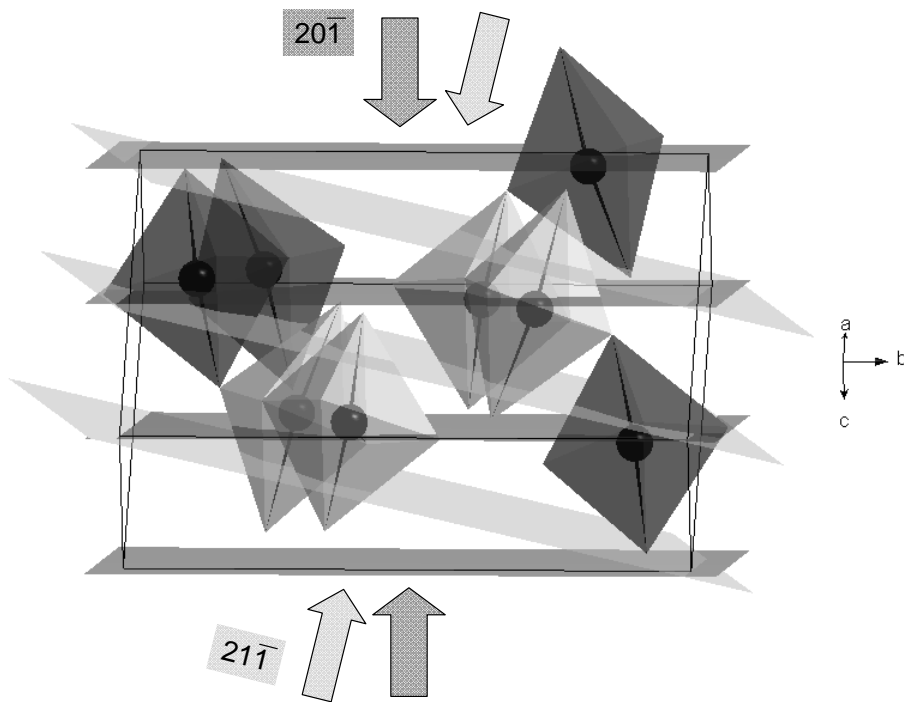


Figure 4

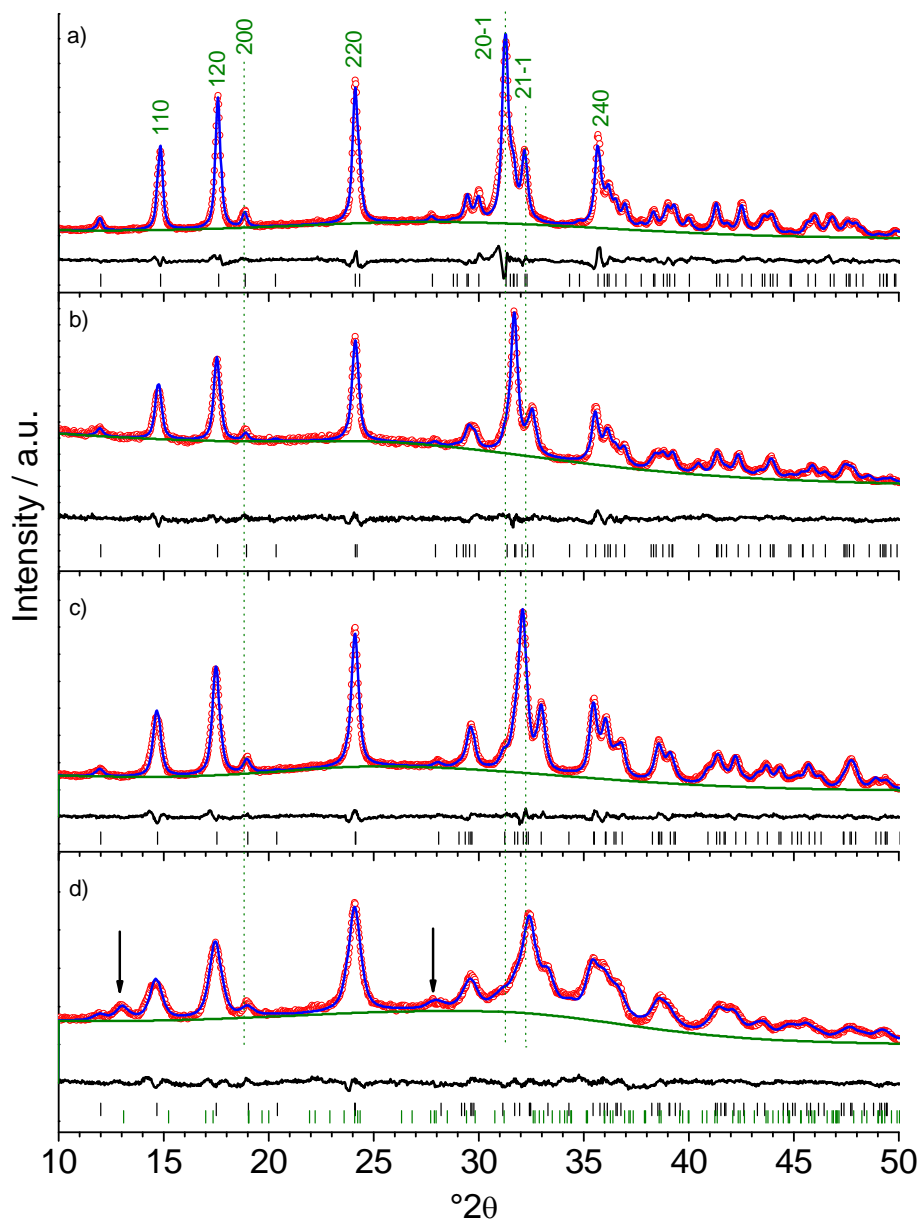


Figure 5

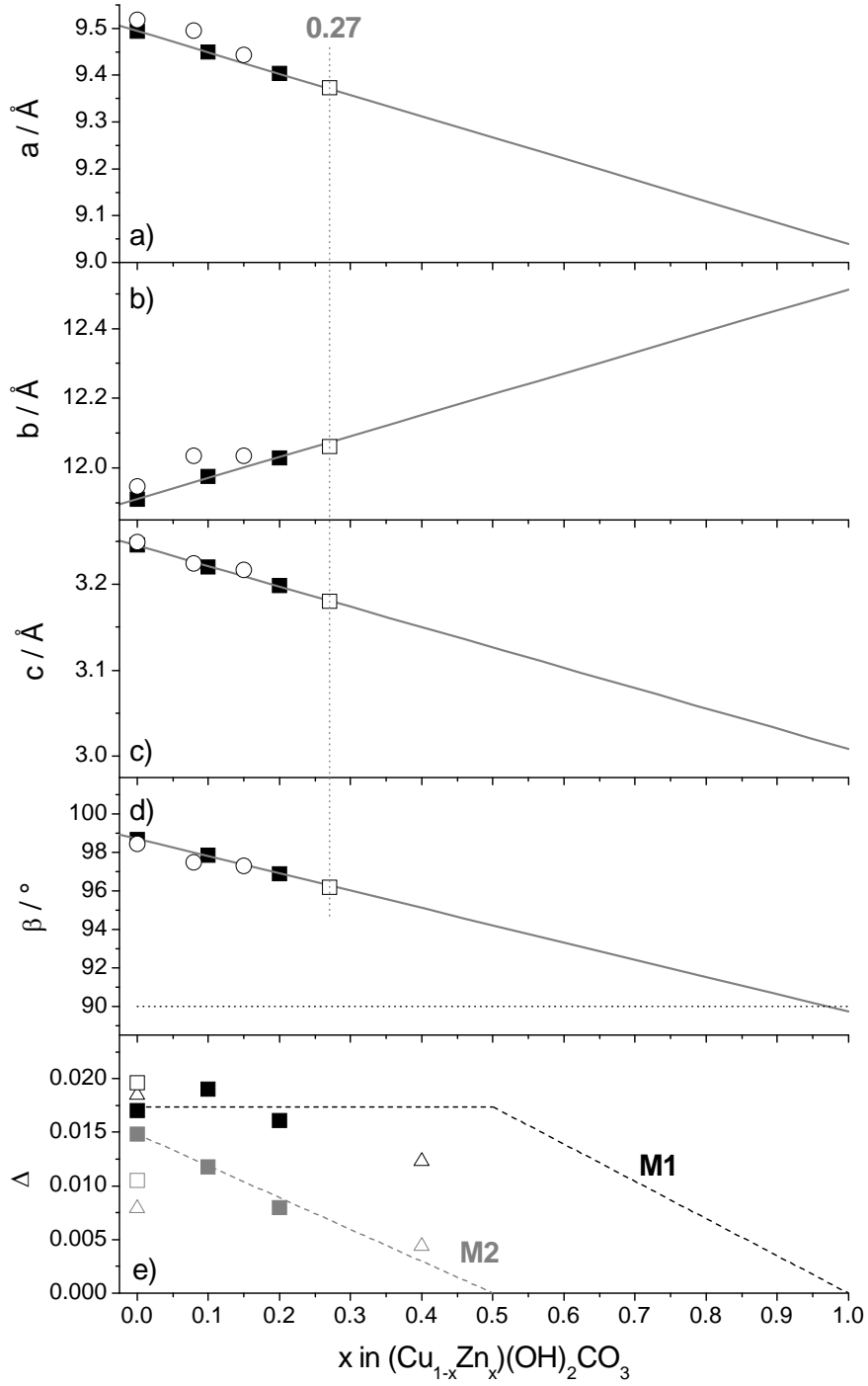


Figure 6

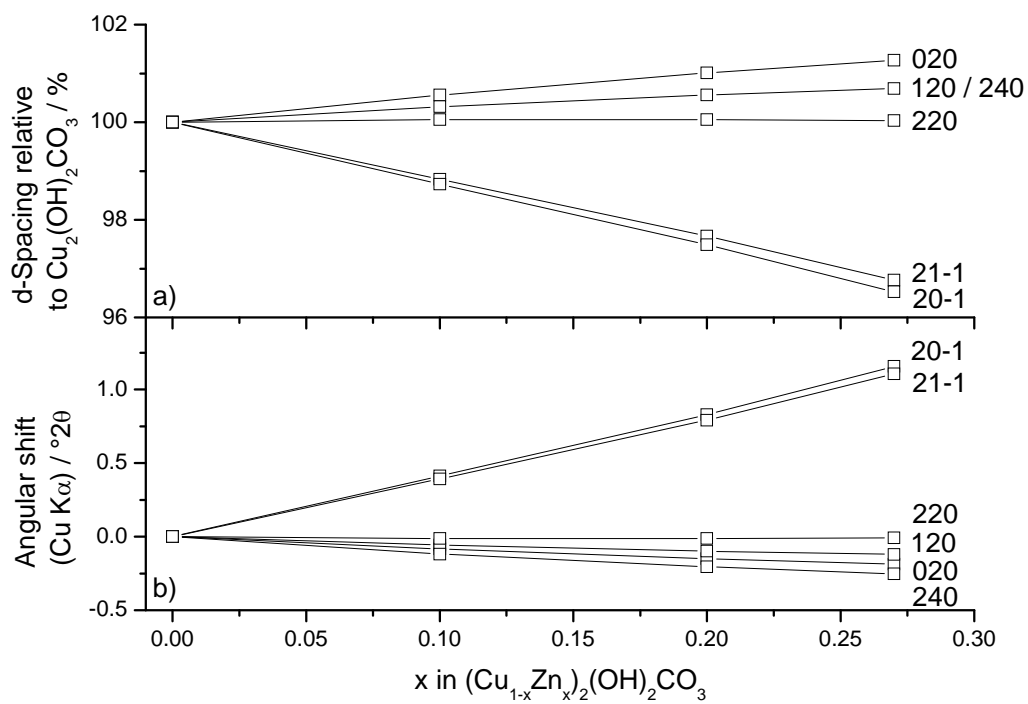


Figure 7

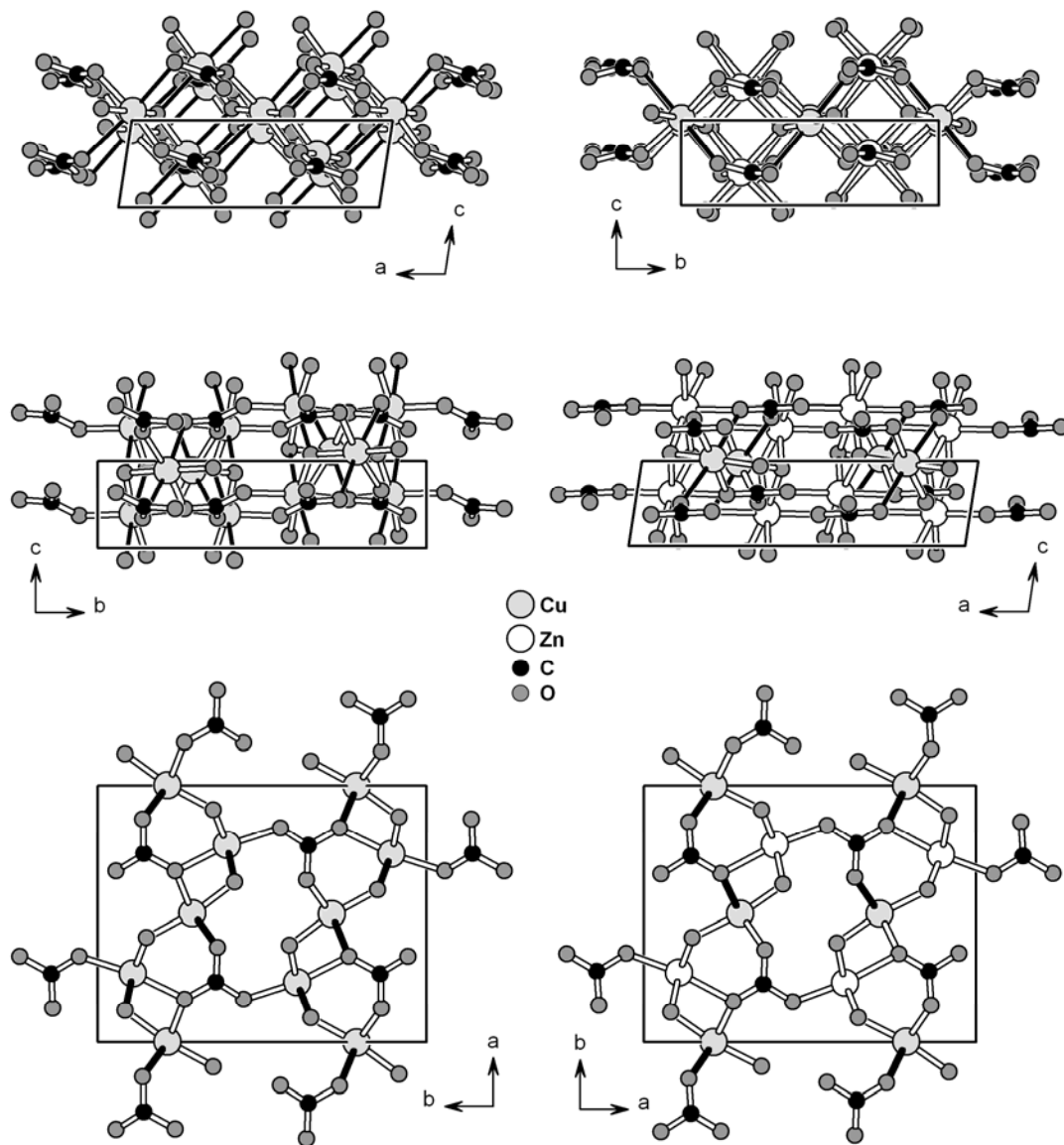


Figure 8

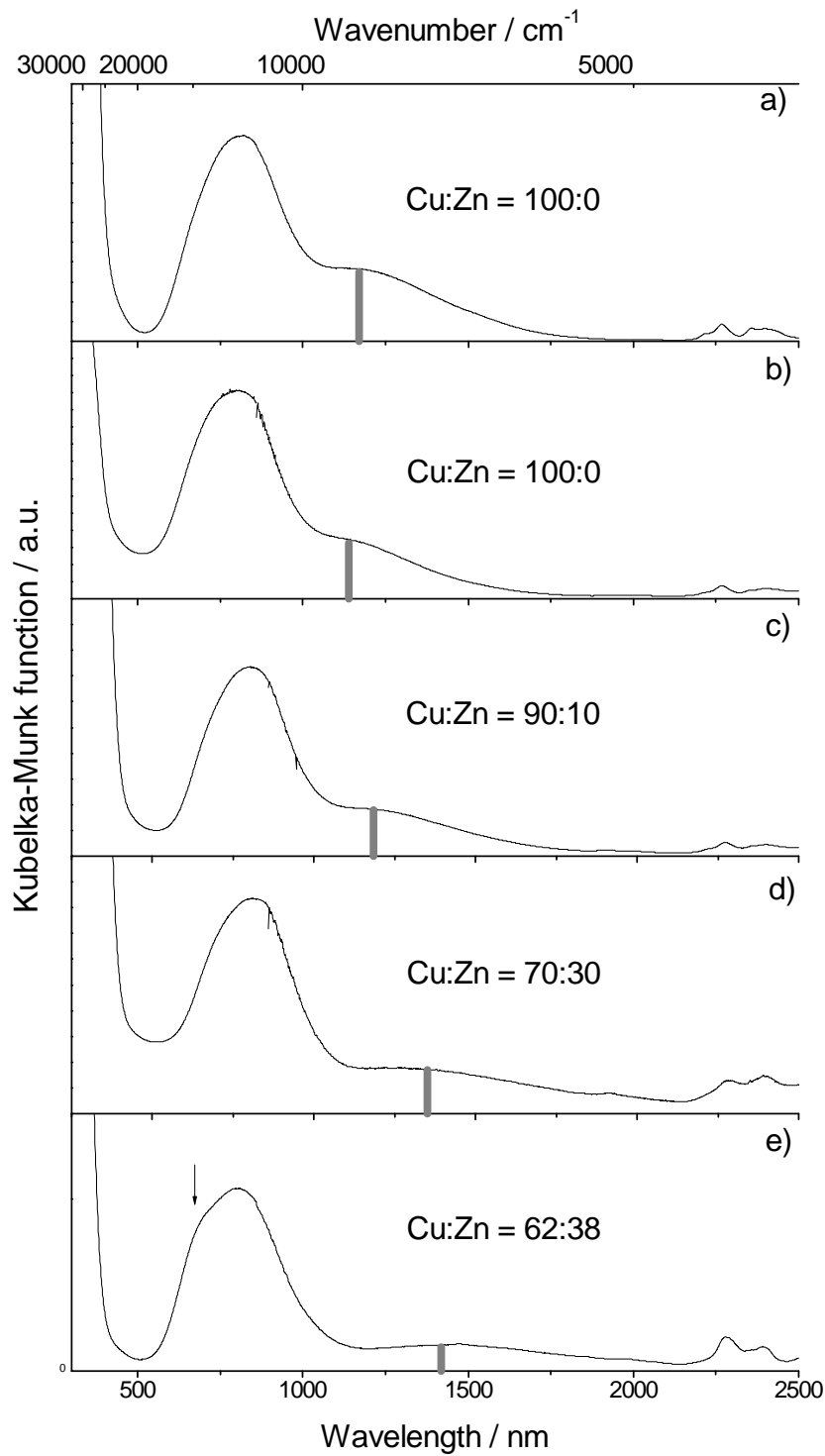


Figure 9

1
2
3
4
5
6
7
8
9
10
11
12
13
14
15
16
17
18
19
20
21
22
23
24
25
26
27
28
29
30
31
32
33
34
35
36
37
38
39
40
41
42
43
44
45
46
47
48
49
50
51
52
53
54
55
56
57
58
59
60

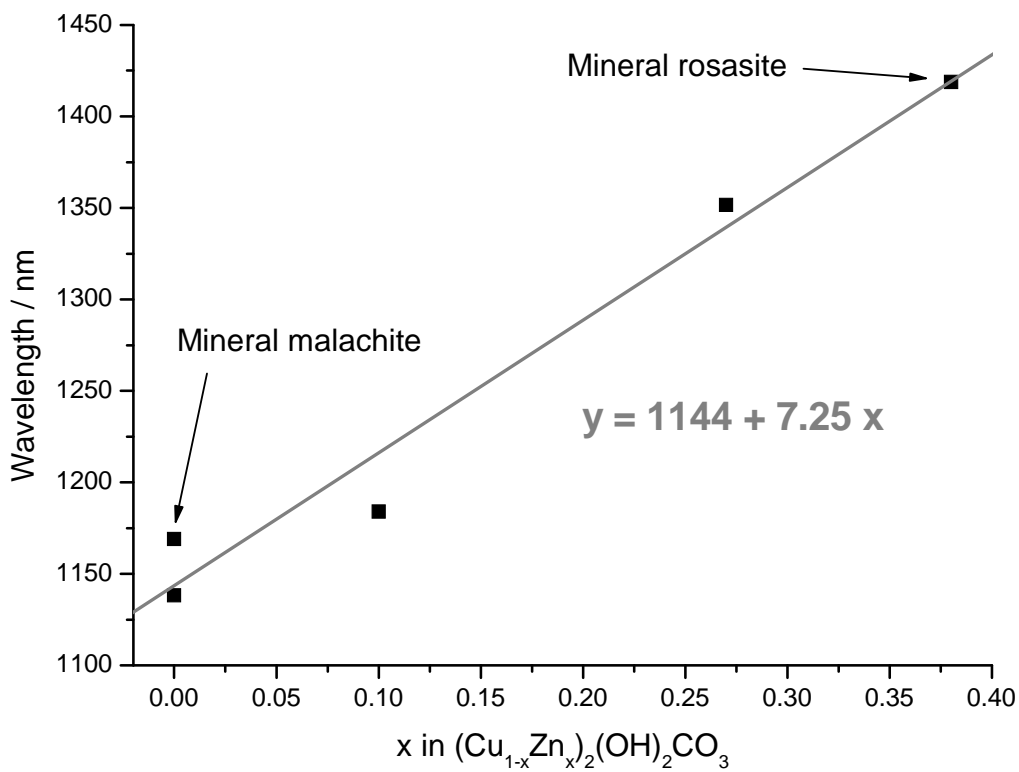


Figure 10

